Journal of
Materials Chemistry A

ROYAL SOCIETY
OF CHEMISTRY

PAPER

View Article Online
View Journal | View Issue

Check for updates

Cite this: *J. Mater. Chem. A*, 2022, **10**, 4428

Processing and characterisation of $BaZr_{0.8}Y_{0.2}O_{3-\delta}$ proton conductor densified at 1200 °C†

Ángel Triviño-Peláez,[a] Domingo Pérez-Coll,[a] Mario Aparicio,[a] Duncan P. Fagg,[b] Jadra Mosa[a] and Glenn C. Mather*[a]

Received 22nd November 2021
Accepted 31st January 2022

DOI: 10.1039/d1ta09998a

rsc.li/materials-a

Barium zirconate-based perovskites (BZY) are intensely studied proton conductors for high-temperature electrochemical applications; however, their refractory nature means excessive temperatures are required for sintering (~1700 °C). Although different strategies have been employed to improve densification, a high-temperature step (1300–1700 °C) is generally required to achieve sufficient grain growth and good electrical properties. Here, sol–gel synthesis using alkoxide precursors is employed to obtain $BaZr_{0.8}Y_{0.2}O_{3-\delta}$ sinter-reactive powders with Ba excess at 750 °C. High relative densities (~98%) of ceramic bodies with an average grain size ~190 nm were obtained on sintering isostatically-pressed pellets at the uniquely low temperature of 1200 °C for 4 hours on addition of 4% mol ZnO as a sintering agent to the Ba-excess sol–gel powders. Impedance spectroscopy indicates that the resistance of the greater grain-boundary volume arising from the low densification temperature is largely offset by a higher specific grain-boundary conductivity than that of the same composition sintered at 1650 °C with larger grain size. Conductivity measurements for prolonged periods in dry and wet (p_{H2O} ~ 0.022 atm) 90% N_2 : 10% H_2 and 90% Ar : 10% CO_2 atmospheres at 500 °C verified that Ba excess in the starting composition did not contribute to deteriorating chemical stability. Processing of sol–gel BZY nanopowders with Ba excess combined with ZnO sintering aid is thus demonstrated as a successful low-temperature route for obtaining BZY with high density, stability and sufficient grain growth for electrochemical applications.

1. Introduction

$Ba(Zr,Y)O_{3-\delta}$ perovskites (BZY) are highly studied candidates for application as electrolytes in protonic ceramic fuel cells (PCFCs) and protonic ceramic electrolyser cells (PCECs) due to their good protonic conductivity in the intermediate temperature range (400–700 °C) and high stability against acidic gases such as CO_2.[1–3] Nevertheless, implementation of BZY in these devices is complicated by its refractory nature, which causes poor densification, low grain growth, and high grain-boundary resistances. Elevated sintering temperatures (~1700 °C) are thus required for fabrication of dense membranes, leading to elemental segregation and barium loss.[4,5] In this respect, poor reproducibility of conductivity has been associated with the uncontrolled Ba stoichiometry arising from high-temperature sintering.[2,6] In addition, the energy requirements and costs for densification of BZY electrolytes at such temperatures impose serious barriers to their use in electrochemical devices at the industrial scale. Due to moderate conductivity, BZY is best suited to thin-film configurations in electrochemical devices where high sintering temperatures can also lead to its reaction with the electrode support.

Hence various strategies have been adopted to lower the temperature and time required for densification and grain growth, including reactive sintering,[7,8] use of dopants,[9] the introduction of sintering aids[10–13] and cold sintering.[14] One of the more studied sintering additives is ZnO as it offers a low sintering temperature (~1300–1350 °C) and is not known to form secondary phases.[10,11,15] In the absence of sintering additives, Babilo *et al.*[6] report that crystallite sizes below 100 nm and excess barium are generally required to achieve good densification, even at a sintering temperature of 1600 °C.

In this respect, sol–gel synthesis has several attractive features, including the formation of fine powders, easy adaptation to thin-film processing and high purity. Here, we report the synthesis of $BaZr_{0.8}Y_{0.2}O_{3-\delta}$ using a sol–gel method employing an alkoxide route to achieve highly sinterable nanopowders at the low temperature of 750 °C. The employment of Ba excess in the initial stoichiometry and addition of ZnO as sintering additive ensure an unprecedented low sintering temperature of 1200 °C for achieving highly dense, stable ceramics. Impedance spectroscopy in a series of wet and dry

---

[a] *Instituto de Cerámica y Vidrio (CSIC), Campus de Cantoblanco, 28049, Madrid, Spain. E-mail: mather@icv.csic.es*

[b] *Centre for Mechanical Technology and Automation, TEMA, University of Aveiro, 3810 193 Aveiro, Portugal*

† Electronic supplementary information (ESI) available. See DOI: 10.1039/d1ta09998a

atmospheres is employed to reveal the grain and grain-boundary electrical properties of samples with low-temperature densification and comparison to analogues with high-temperature sintering is made.

2. Experimental

$BaZr_{0.8}Y_{0.2}O_{3-\delta}$ (BZY20), both with and without nominal 10 at% Ba excess, was prepared by a sol–gel processing route based on alkoxide precursors in a manner similar to that described recently for the related $SrZrO_3$-based perovskite.[16] The following starting reagents were employed: zirconium(IV) propoxide ($Zr(OC_3H_7)_4$) (Sigma-Aldrich, 70% in 1-propanol), yttrium(III) butoxide ($Y(OC_4H_9)_3$) (Sigma-Aldrich, 0.5 M in toluene) and barium (Sigma-Aldrich, 99%); 2-methoxyethanol (Sigma-Aldrich, anhydrous, 99.8%) and deionized water were used as ion-exchange medium and for hydrolysis, respectively. Synthesis was performed under an argon atmosphere in a glove box with strictly controlled conditions of humidity. The molar ratios of Ba : yttrium(III) butoxide : zirconium(IV) propoxide : 2-methoxyethanol : water were 1 : 0.2 : 0.8 : 60 : 3 (stoichiometric Ba) and 1.1 : 0.2 : 0.8 : 60 : 3 (Ba excess).

Powders with and without the additions of Ba excess and 4 mol% of $Zn(NO_3)_2\cdot 6H_2O$ (Alfa Aesar, 99.998%) as sintering aid were ground in a Fritsch Pulverisette 6 planetary ball mill for 2 h at 600 rpm and sieved (100 μm). Powders were shaped into cylindrical pellets by uniaxial pressing to 37.5 MPa then isostatic pressing to ~196–294 MPa (~2000–3000 kg cm^{-2}) followed by sintering at temperatures in the range 1100–1650 °C for 4 h in air. The evolution of the sol–gel reaction was evaluated by X-ray diffraction (XRD) using a Bruker D8 high-resolution diffractometer (monochromatic Cu $K\alpha_1$ radiation, $\lambda = 1.5406$ Å) over the range $15° \leq 2\theta \leq 100°$, employing a step width of 0.02° and 0.8 s per step. Material was prepared for Rietveld refinement by removing the surface layer from sintered samples prior to grinding to a fine powder. Crystallite size, ϕ, was calculated from the X-ray diffraction powder profiles after calcining at 750 °C in argon employing the Scherrer formula:

$$\phi = \frac{0.94 \times \lambda}{\cos(\theta) \times \sqrt{B^2 - B_i^{\,2}}} \tag{1}$$

where θ corresponds to the angle of the most intense diffraction peak of the perovskite phase, B is the full width at half maximum, and B_i is the instrumental broadening; the constant value of 0.94 is a common factor used for spherical crystals.[17] Rietveld refinement and peak fitting were performed with the Fullprof software, employing a pseudo-Voigt profile function.[18]

The microstructures of fracture surfaces were examined with a Hitachi S-4700 field-emission scanning electron microscope. The densities of sintered pellets for electrical measurements were determined by careful measurement of the mass and geometrical volume; relative density was then calculated as a percentage of the theoretical X-ray density. Densification was also assessed by dilatometry performed with a Setaram Setsys instrument (France) in the range RT–1500 °C in air with a heating rate of 5 °C min^{-1} on pressed pellets from powders treated at 750 °C with and without additions of 4 mol% $Zn(NO_3)_2\cdot 6H_2O$ and Ba excess in the starting stoichiometry.

Electrodes for electrical measurements were prepared by coating polished pellet surfaces with Pt paste (Metalor) followed by firing at 950 °C for 1 h. Impedance spectroscopy was performed with an Autolab PGStat302N-FRA2 instrument operating in the frequency range $0.1 \leq f \leq 10^6$ Hz with a signal amplitude of 50 mV. Conductivity as a function of temperature was recorded in the temperature range 150–950 °C on cooling in steps of 50 °C with a cooling rate of 5 °C min^{-1} and an equilibration time of at least 45 minutes (higher temperatures) and up to 1 h 30 min (lower temperatures) at each temperature in wet and dry flows of O_2, N_2 and $10\%H_2 : 90\%N_2$ regulated by Bronkhorst electronic mass-flow controllers. Dry environments were achieved on flowing the gases through a drying column with a packed bed of commercial aluminosilicate and zeolite beads (Supelco); wet atmospheres ($p_{H_2O} \sim 0.022$ atm) were obtained on bubbling gases through KBr-saturated H_2O at room temperature. Impedance spectra were analysed with the Zview 2.9c program (Scribner Associates), employing equivalent circuits composed of bulk, grain-boundary and electrode processes according to the impedance contributions indicated by the capacitance values.[19]

Stability was assessed under dry and wet ($p_{H_2O} \sim 0.022$ atm) atmospheres of $90\%Ar–10\%CO_2$ and $90\%N_2–10\%H_2$ at 500 °C for prolonged periods on monitoring the impedance response followed by post-operation analysis by XRD. Evaluation of chemical and mechanical stability in laboratory air for up to 14 days was also undertaken for dense sintered pellets which were previously cracked to reveal fresh fracture surfaces. After the exposure period, samples were milled and analysed by XRD.

3. Results and discussion

3.1 Sol–gel synthesis

A schematic illustration of the synthesis procedure is shown in Fig. 1. Barium filings were dissolved in 2-methoxyethanol while stirring at room temperature under an argon atmosphere for 3 hours to form barium alkoxide. The homogeneous, transparent and precipitate-free solution of barium alkoxide, Fig. 1, indicated that barium is completely retained in the matrix and pure alkoxide is obtained. An excess of 2-methoxyethanol was employed to ensure complete reaction to the alkoxide as follows:[20]

$$Ba + 2(CH_3OCH_2CH_2OH) \rightarrow Ba(O_2C_3H_7)_2 + H_2(g)\uparrow \tag{2}$$

Zirconium(IV) propoxide and yttrium(III) butoxide were added to the solution to achieve a complete homogeneous mixture of triple alkoxide by stirring for 2 hours at room temperature. After stirring the solutions for 30 min at room temperature, a second solution of 2-methoxyethanol and water was then added dropwise to promote hydrolysis and condensation reactions. Homogeneous, transparent solutions were obtained after mixing for 3 hours at room temperature. Operation in an inert environment is required to prevent formation of precipitates in

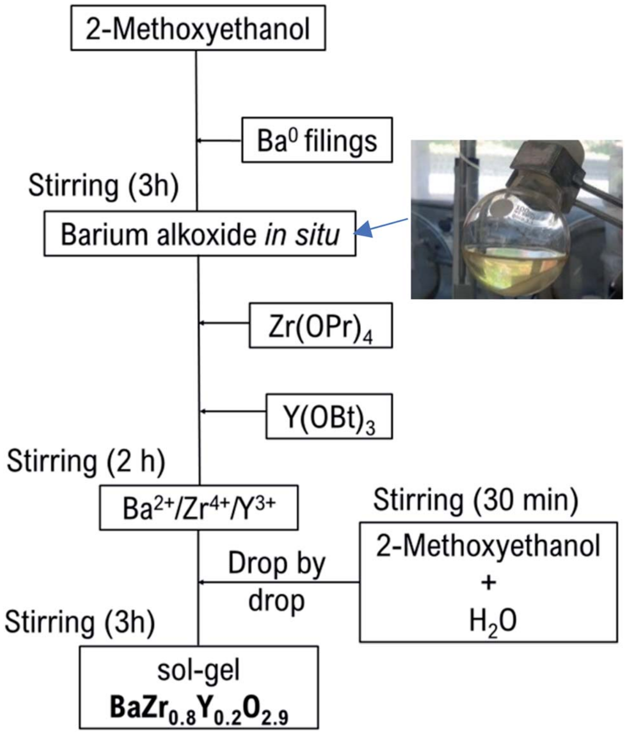

Fig. 1 Synthesis scheme of the sol–gel preparation of the BZY20 using alkoxide precursors.

the reagent matrix and favour high purity of the final product. Solvents were removed in a rotavapor by vacuum distillation, yielding a very viscous caramel-like, dark-orange gel. The gel was combusted at 350 °C then 750 °C under argon for 4 h at each temperature to ensure the complete elimination of synthesis alcohols, with an intermediate step of grinding the product in an agate mortar, leaving a light-grey powder.

3.2 Phase formation, densification and microstructure

XRD patterns of the sol–gel powder treated at 500 °C (not shown) indicated that the material was still highly amorphous at this temperature. Moreover, DTA (not shown) indicated that expulsion of organic products was only complete at 750 °C, hence this temperature was adopted for treatment of the sol–gel powders prior to densification at higher temperature. Formation of perovskite BZY20 was confirmed by XRD on thermal treatment of the sol–gel powder at 750 °C under an Ar atmosphere. A minor amount of $BaCO_3$ was discerned for both nominally stoichiometric and superstoichiometric Ba starting concentrations at this temperature. The XRD data of the powder with Ba excess were employed for Rietveld refinement in the cubic $Pm\bar{3}m$ space group, Fig. 2(a), which indicated that 3.7 wt% $BaCO_3$ was present; we note that vestiges of $BaCO_3$ were also discerned in the Ba-stoichiometric analogue. The cubic lattice parameter of the BZY-based phase prepared at 750 °C (a = 4.2035(2) Å) was first determined on refining the structure with the addition of CaF_2 as internal lattice-parameter standard then was held constant in a second refinement without addition of the standard, shown in Fig. 2(a); a comparison of lattice parameters for selected samples is provided in Table S1.† The average crystallite size of BZY20 as determined from the XRD diffraction profiles with the Scherrer equation was 32 nm. A scanning electron micrograph of the sol–gel powder treated at 750 °C, Fig. 3(a), confirms the nanometric size of the agglomerated crystallites.

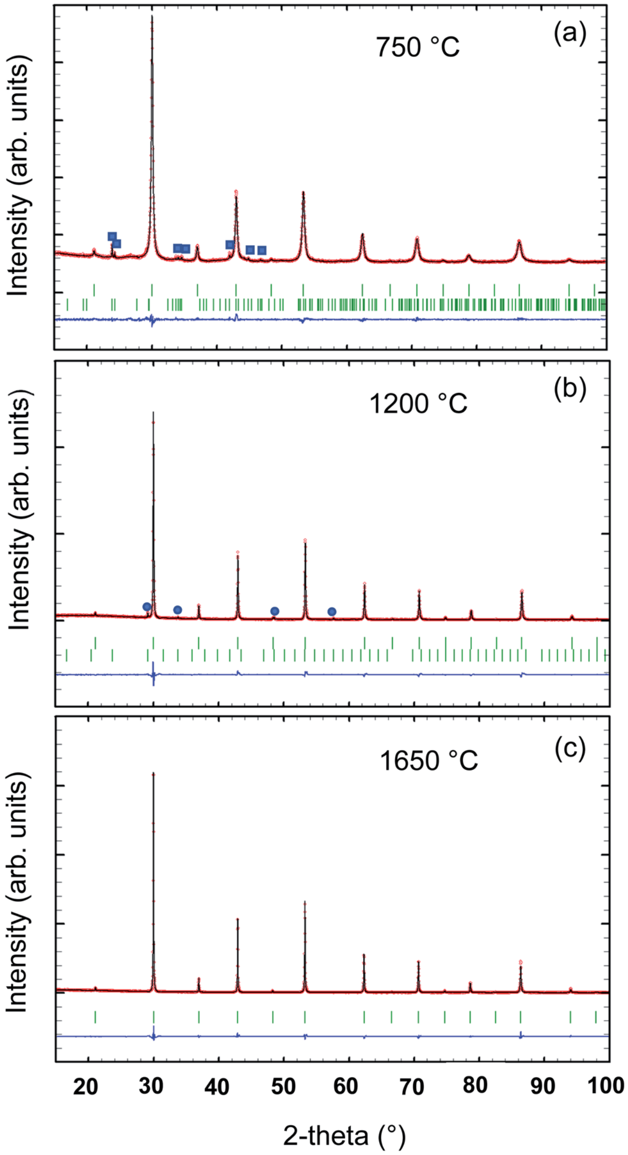

Fig. 2 XRD Rietveld refinement plots showing observed (red circles), calculated (continuous black line) and difference (continuous blue line at bottom) diffraction profiles of (a) BZY20 powder heat treated at 750 °C for 4 hours under an Ar atmosphere showing $BaCO_3$ peaks as squares (space group *Pmcn*); (b) BZY20 sintered at 1200 °C for 4 hours showing Y_2O_3 peaks as circles (space group, $Ia\bar{3}$); (c) BZY20 sintered at 1650 °C for 4 hours. Top and bottom vertical bars indicate the expected position of Bragg peaks of the simple cubic perovskite phase (space group, $Pm\bar{3}m$) and second phase, respectively.

Addition of 4 mol% ZnO as sintering aid to the sol–gel nanopowder with Ba excess followed by isostatic pressing then sintering at 1200 °C for 4 hours produced ceramic bodies with a relative density (r.d.) of 98%. The temperature dependence of

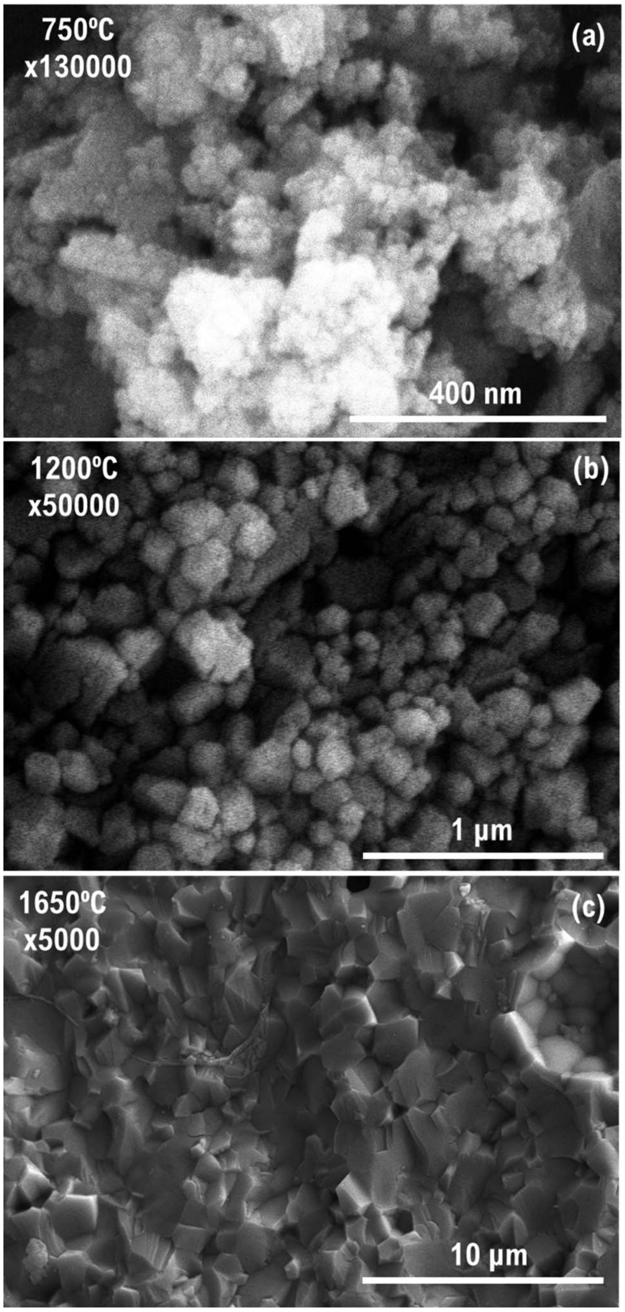

Fig. 3 SEM images of (a) sol gel powder of BZY20 heat treated at 750 °C; fracture surfaces of sol–gel prepared BZY20 with Ba excess and ZnO sintering aid sintered at (b) 1200 °C for 4 hours and (c) 1650 °C for 4 hours.

densification as determined by dilatometry for the as-prepared nanopowder with and without Ba excess (10 at%), and with addition of ZnO (4 mol%) as sintering agent are shown in Fig. 4. It is observed that independent addition of either ZnO or Ba excess promotes greater linear shrinkage in comparison to the stoichiometric BZY20 sol–gel sample. However, the combination of Ba excess and ZnO additive results in a clear improvement of shrinkage at lower temperature, as is apparent from the onset of the abrupt stage of densification at around 1200 °C.

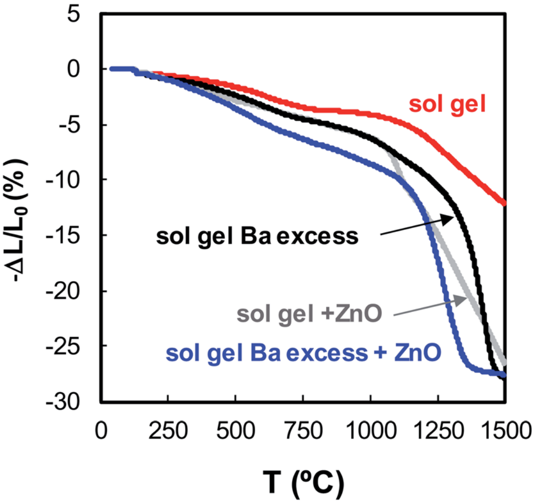

Fig. 4 Temperature dependence of densification of sol–gel prepared BZY20 nanopowders showing effects of additions of nominal Ba excess and ZnO as sintering aid.

Preparation of the sol–gel material with the nominally stoichiometric amount of Ba led to much lower densities; hence, these compositions were not studied further. BZY20 densified at 1200 °C with Ba excess and ZnO sintering agent (BZY20-1200) was also fired at 1650 °C for 4 hours to promote grain growth and determine the effects of the different grain sizes associated with the respective sintering temperatures on the electrical properties (BZY20-1650). The corresponding scanning electron micrographs of fracture surfaces of material sintered at 1200 °C and 1650 °C for 4 hours are shown in Fig. 3. Grain size was calculated to be 190 nm and 1.4 µm for samples sintered at 1200 and 1650 °C, respectively.

The observed XRD profile of BZY20 sintered at 1200 °C and the difference between observed and calculated patterns as determined by Rietveld refinement are shown in Fig. 2(b); the corresponding structural parameters and agreement factors are shown in Table S2.† Vestiges of Y_2O_3 (2.8 wt%) were discerned in the XRD patterns of samples treated at 1200 °C but $BaCO_3$ was no longer detected. The lattice parameter increased to 4.20521(4) Å on firing at 1200 °C, which is attributable to increasing reaction with $BaCO_3$. It has previously been shown that the lattice parameter of BZY20 goes through a maximum, increasing up to 1250 °C due to greater reaction with $BaCO_3$, after which the cell parameter then decreases due to Ba loss.[5] Yttria is a common second phase on high-temperature and prolonged sintering of BZY due to Ba loss occurring above 1250 °C.[5,21] However, its presence in the composition with Ba excess sintered at the low temperature of 1200 °C is somewhat unexpected. Moreover, the material sintered at 1650 °C was free of Y_2O_3 (Rietveld refinement plots shown in Fig. 2(c), and corresponding structural parameters and agreement factors in Table S2†) indicating that the presence of Y_2O_3 at the lower temperature is likely to result from kinetic factors. Since some Ba is present in the form of $BaCO_3$ at the lower temperature of 750 °C, but no yttria-based phase is discerned at this temperature, a minor amount of Y must occupy the A site, which is more favourable than the formation of Ba vacancies in barium zirconate.[4] On sintering at 1200 °C, Ba then displaces the A-site Y, which forms Y_2O_3 as a second phase. At the higher temperature of 1650 °C, the lattice parameter of the sample again increases to 4.21102(5) Å, indicating that further incorporation of Ba on the A site, along with incorporation of Y from the secondary phase on the B site, takes place. Both substitution mechanisms would increase the average ionic radii of the two sites leading to a greater lattice parameter. This suggests that some Ba is still present in amorphous form at 1200 °C. Any B-site cation excess which can give rise to the presence of Y_2O_3 on high-temperature sintering may not occur in the present case due to the initial Ba superstoichiometry, as occurs for BZY samples covered with $BaCO_3$,[21] or because sintering at the high temperature is not performed long enough to observe substantial yttria precipitation.[5] It should be noted that the presence of such a minor amount of Y_2O_3 on sintering at 1200 °C does not have a detrimental effect on the electrical properties, as described in the next section.

It is also of note that no ZnO or Zn-containing second phases are observed in the XRD patterns of the samples sintered at 1200 °C. The addition of Zn in the manner adopted in the present study corresponds to a B-site cation excess in the case of nominally stoichiometric Ba; however, in the case of Ba excess, its addition may be considered to occur *via* a B-site cation substitution mechanism. It has recently been shown that, for such a mechanism, Zn is likely to be located in both the grain and grain boundary,[22] hence its absence in the XRD patterns as a second phase. We may also note that no other phase involving reaction of Zn and Ba appears at the resolution of XRD. Addition of Zn to BZY generally lowers the lattice parameter of the parent phase. However, in the present case, the lattice parameter is higher for the samples sintered at 1200 °C with addition of ZnO in comparison to the ZnO-free nanopowder treated at 750 °C since, as mentioned, the excess Ba observed at 750 °C is incorporated in the structure at the higher temperature, outweighing the contraction expected from the incorporation of Zn.

In addition to the dilatometry study (Fig. 4), sintering of samples both with and without ZnO and with and without Ba excess at isothermal plateaux in the range 1200–1300 °C for 4 hours indicated that high relative densities at 1200 °C (98%) were only obtained on incorporation of both Ba excess in the starting composition and ZnO as sintering additive. A lower temperature of 1100 °C proved insufficient to achieve high densification even with excess Ba and ZnO as sintering aid. Yamazaki *et al.*[7] reported the formation of dense BZY with large grain size on sintering nanoscaled precursor powder with Ba excess but at the much higher sintering temperature of 1600 °C; nevertheless, the carbonate disappeared in XRD patterns of sample treated at 1200 °C, as occurs in the present study. $BaCO_3$ is suggested to decompose and react with the perovskite phase on sintering (reactive sintering) *via* the presence of a liquid phase which may lower sintering and enhance grain growth. Cervera *et al.*[23] employed nanograined powders (3–5 nm) and extreme pressures (4 GPa) to densify compacts with high relative density at low temperature (98.1% r.d. at 1250 °C) at the expense of a high grain-boundary volume (grain size, ~50 nm), and a subsequent high-temperature sintering step was required to achieve competitive conductivity levels. Hence, the presence of $BaCO_3$ in the pre-sinter composition appears to play a crucial role in obtaining sufficient densification and grain growth at low temperature both in our study and that of Yamazaki *et al.* However, the low densification temperature and grain size of 190 nm attained in the present study is only achieved with the presence of both Ba excess and addition of the well-studied ZnO sintering aid to the BZY nanopowders.

A number of mechanisms have been proposed for incorporation of Zn in BZY, which include substitution on the B site with creation of A-site vacancies:[10]

$$\mathrm{ZnO} \xrightarrow{\mathrm{BaZrO_3}} \mathrm{Zn}''_{\mathrm{Zr}} + 2\mathrm{V}^{\bullet\bullet}_{\mathrm{O}} + \mathrm{O}^{\times}_{\mathrm{O}} + \mathrm{V}''_{\mathrm{Ba}} \tag{3}$$

This may be accompanied by dopant partitioning such that Y^{3+} occupies by both A and B sites:[24,25]

$$2\mathrm{Ba}^{\times}_{\mathrm{Ba}} + 2\mathrm{O}^{\times}_{\mathrm{O}} + \mathrm{Y}'_{\mathrm{Zr}} + \mathrm{V}^{\bullet\bullet}_{\mathrm{O}} \rightarrow \mathrm{Y}^{\bullet}_{\mathrm{Ba}} + 2\mathrm{BaO} \tag{4}$$

$$\left(\mathrm{V}'''_{\mathrm{Zr}} + \mathrm{V}''_{\mathrm{Ba}} + 3\mathrm{V}^{\bullet\bullet}_{\mathrm{O}} \rightarrow \mathrm{null}\right)$$

Note that these mechanisms lead to creation and consumption of oxygen vacancies, respectively.[22] Alternatively, the ZnO may remain as a second phase or form clusters with Ba vacancies[26]

$$\mathrm{ZnO} + \mathrm{V}''_{\mathrm{Ba}} + V^{\bullet\bullet}_{\mathrm{O}} \rightarrow (\mathrm{Zn_i} \times V_{\mathrm{Ba}})^{\times} + O^{\times}_{\mathrm{O}} \tag{5}$$

We recently demonstrated that, for a number of different Zn substitution mechanisms, addition of ZnO promotes high densification levels.[22]

3.3 Phase stability

Perovskite proton conductors with Ba as the A-site cation exhibit poor stability related to carbonation in CO_2-containing atmospheres. The endothermic nature of the reaction means that carbonation can readily occur in atmospheric air at room temperature.[27,28] Moreover, unreacted BaO typically residing in the grain boundaries may react with CO_2 leading to the degradation of sintered bodies. The increasing lattice parameter observed between the samples sintered at 1200 and 1650 °C suggests that further Ba is incorporated into the structure at the higher temperature and that Ba must still be present in an amorphous form at the lower temperature. To assess the stability of the material sintered at 1200 °C with nominal Ba excess in the starting composition, conductivity measurements in dry and wet ($p_{H2O} \sim 0.022$ atm) atmospheres of 90%Ar–10% CO_2 and 90%N_2–10%H_2 were performed. Fig. 5(a) shows that the total conductivity of BZY20-1200 at 500 °C in the CO_2-containing atmosphere decreases ~4% from its initial conductivity after a period of ~80 hours, then remains relatively stable. Conductivity was also recorded for 4 days in 90%N_2–10%H_2 at

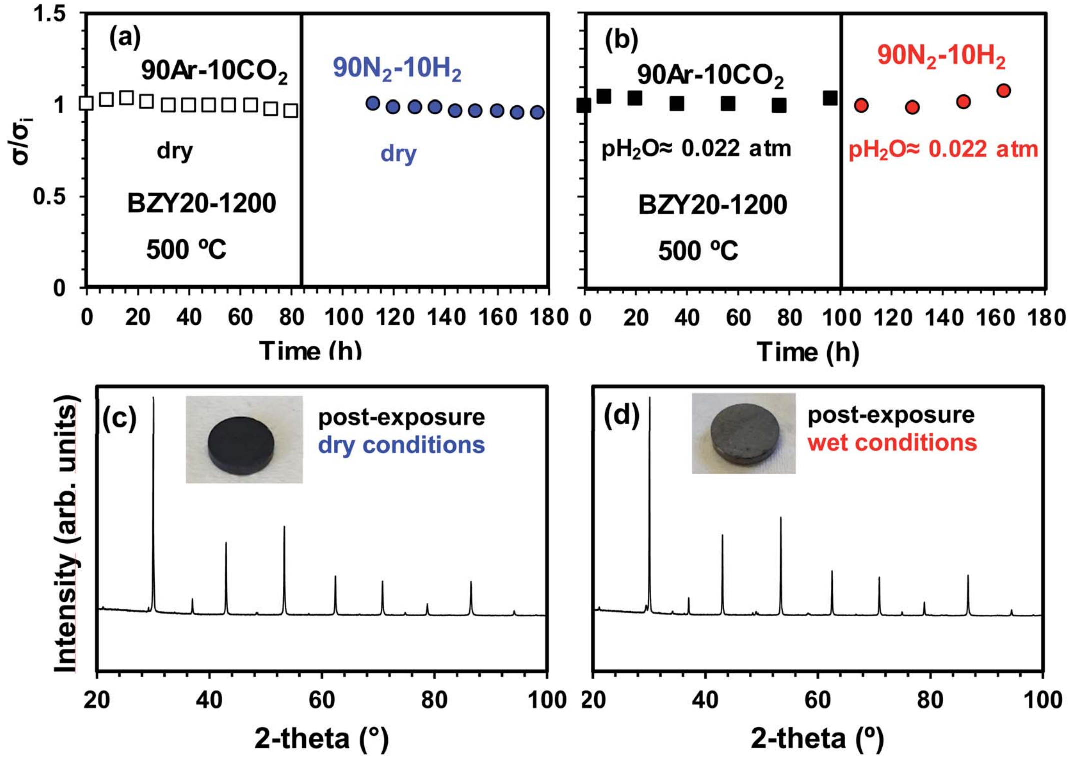

Fig. 5 (a) Fraction of initial conductivity as a function of exposure time for sol–gel prepared BZY20 with Ba excess and ZnO sintering aid sintered at 1200 °C exposed to atmospheres of (a) dry 10% CO_2 : 90% Ar then 10% H_2 : 90% N_2, and (b) wet ($p_{H_2O} \sim 0.02$ atm) 10% CO_2 : 90% Ar then 10% H_2 : 90% N_2; (c) XRD pattern of sample "post operation" after exposure to dry 10% CO_2 : 90% Ar and 10% H_2 : 90% N_2 and (d) XRD pattern of sample "post operation" after exposure to wet 10% CO_2 : 90% Ar and 10% H_2 : 90% N_2; insets show corresponding photographic images of pellet "post exposure" in dry and wet conditions.

500 °C. After an initial period of stabilisation in the same atmosphere for 28 h, Fig. 5(a), the conductivity dropped by ∼5% with respect to the starting value. The mechanical integrity of the sample was retained after the exposure period to the dry CO_2- and H_2-containing atmospheres (inset of Fig. 5(c)) and XRD of the milled sample indicated that no reaction had taken place (Fig. 5(c)). The analogous experiment performed in wet 90%Ar–10%CO_2 followed by wet 90%N_2–10%H_2 indicated similarly good stability in the wet CO_2-containing atmosphere with conductivity essentially invariant after 100 hours; on transitioning to wet 90%N_2–10%H_2, the conductivity also remains stable; note that there is some observable oscillation in the data in wet conditions, most likely due to the varying room temperature of the bubbler system during daytime and night-time measurements. Mechanical integrity was maintained (inset of Fig. 5(d)) after exposure to the humid conditions and the corresponding XRD pattern of the milled sample (Fig. 5(d)) indicated no evidence of carbonate or hydroxide formation.

Considering that carbonation is thermodynamically more favourable at low temperatures, a further test of stability involved exposure of dense pellet fragments to laboratory air for a period of 14 days. Similar studies have shown degradation of $BaCeO_3$-based phases, readily apparent on visual inspection, resulting in mechanical breakdown of sintered bodies.[27] No visual evidence of carbonate formation was observed after the exposure period, Fig. S1,† and mechanical integrity was retained. Moreover, XRD powder patterns (not shown) of the pellet fragments subsequent to the exposure indicated an absence of carbonation products. Hence, the Ba excess employed in the starting stoichiometry to improve densification does not promote carbonation and mechanical degradation.

3.4 Electrical properties

Fig. 6 shows the impedance spectra of BZY20-1200 and BZY20-1650 in wet N_2 at 150, 250 and 350 °C. The impedance response ascribed to grain and grain-boundary processes presents very interesting features, which have been subject to different interpretations in the literature. This has, most probably, been partially responsible for the considerable scattering of reported conductivities of BZY. Both samples show several contributions to the impedance spectra, corresponding to high-, intermediate- and low-frequency processes. The spectra were fitted according to several R_iQ_i terms located in series to account for each impedance response, where R_i and Q_i correspond to the resistance and constant-phase-element of the specific process. The high-frequency contribution is only manifested at very low temperature (150–200 °C), with values of capacitances of the order of $\sim 10^{-12}$ F cm^{-1} for both samples, and can be assigned to the bulk process (Fig. 6(a) and (d)). As temperature increases, the bulk response is represented as a displacement from the origin of the whole spectra on the real axis (Fig. 6(b)–(f)), since

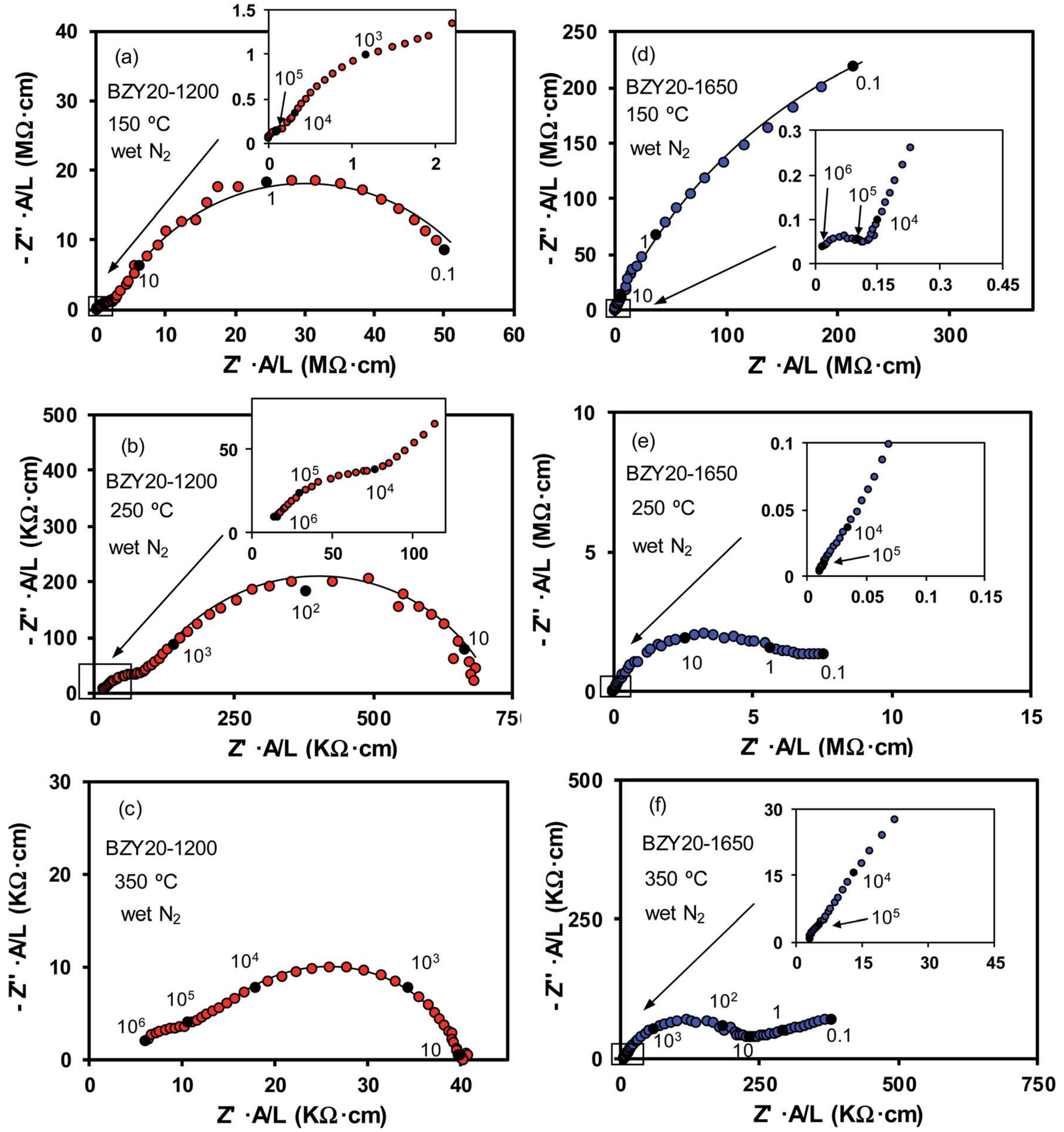

Fig. 6 Impedance spectra collected in humidified N_2 for BZY20 sintered at 1200 °C (BZY20-1200, a–c) and BZY20 sintered at 1650 °C (BZY20-1650, d–f) at 150 °C (a and d), 250 °C (b and e) and 350 °C (c and f). Insets in the figures correspond to magnifications in the high-frequency range. Selected reference frequencies are indicated.

the higher relaxation frequency associated with the lower resistance is beyond the instrumental measurement limits.

The lower-frequency processes exhibit different features for the samples sintered at 1200 and 1650 °C. BZY20-1200 presents two clearly resolved contributions between 150–400 °C (Fig. 6(b) and (c)), with capacitances of the order of $\sim 10^{-10}$ and 10^{-9} F cm^{-1}, respectively, for the intermediate- and low-frequency responses. In contrast, the BZY20-1650 sample presents a distorted arc in the intermediate-low frequency region (Fig. 6(e) and (f)), which is characterised by two different *RQ* processes with similar capacitances to those of the BZY20-1200 sample. It is notable that, for BZY20-1650, the process with capacitance of the order of $\sim 10^{-9}$ F cm^{-1} has a higher resistance in comparison to that of capacitance $\sim 10^{-10}$ F cm^{-1}. The presence of these overlapped responses in the intermediate- and low-frequency zones has previously been observed in similar BZY compositions at low temperatures[21,29] and for other doped Ba-zirconates,[30] although there is some ambiguity regarding the assignation of the corresponding processes. Babilo *et al.*[21] studied the lower-frequency processes with different current-collector materials and concluded that the electrochemical process at the electrode could be incorrectly attributed to the grain-boundary response, leading to a significant over-estimation of the electrolyte resistance. On the other hand, Kjølseth *et al.*[29] and Magrasó *et al.*[30] ascribed both the intermediate- and low-frequency processes to the grain boundary.

The values of capacitances (~ 10^{-10} and 10^{-9} F cm^{-1}) obtained in the current work indicate that neither contribution may be attributed to electrochemical processes at the electrode-material interface, which are expected to have higher capacitance values.[31] As regards two different grain-boundary processes contributing to the electrical transport, Fleig[32] reported the analysis of the effect produced by non-ideal microstructures on the impedance spectra. He found that imperfections of the grain-boundary properties can play an important role in real ceramics, producing distortions in the impedance response ascribed to the grain boundaries. This was particularly apparent for samples with a distribution of different grain-boundary conductivities, including a bimodal distribution characterised by a set of grain boundaries with an ideal conductivity and a second set of highly resistive grain boundaries. In the current work, it is likely that vestiges of both Ba and Zn, added as excess dopants, remain as segregated species at the grain boundaries, whose influence is also likely to depend on thermal treatment. This leads to the possibility of a distribution of grain-boundary resistivities at the space-charge zone, which distorts the grain-boundary impedance response and/or the presence of two overlapped arcs in the corresponding impedance region.[32] Fig. 7 shows the Arrhenius representation of total electrical conductivity and the contributions from grain and total apparent grain boundary for BZY20-1200 and BZY20-1650 in dry oxygen. Total conductivity is completely governed by the grain-boundary component for both compositions in the low-temperature range, as is expected as a result of the highly resistive grain boundaries of BZY.[2] As temperature rises, the contribution from the bulk process increases, due to the lower activation energy of the bulk in comparison to that of the grain boundary. The dominance of the grain boundary extends to a slightly higher temperature (~500 °C) in the BZY20-1650 sample compared to that of BZY20-1200 (~350 °C). Although deconvolution of the impedance spectra into bulk and grain-boundary processes is not possible at high temperature, it is expected from Fig. 7 that total conductivity above 600 °C corresponds to the bulk component, with values of 1.8×10^{-3} and 1.4×10^{-3} S cm^{-1} registered for BZY20-1200 and BZY20-1650, respectively. Table 1 lists the values of conductivity obtained in the current work compared to previously reported values in the literature in various atmospheres and for different sintering temperatures. Note that the conductivity at 600 °C in oxidising atmospheres is affected by the electron–hole contribution, which has a direct impact on the increase of total conductivity. Although the majority of reported values are of the order of 10^{-3} S cm^{-1} in wet reducing atmospheres, in good agreement with our results, some reported conductivities are several times higher. This discrepancy may be partially associated with the correct identification of the grain boundary and its contribution to the total resistance. Nevertheless, conductivities as high as 10^{-2} S cm^{-1} at 600 °C, where the total conductivity is mainly governed by the bulk component, have been reported, exceeding the bulk conductivity obtained in the current work and that previously reported by other authors (Table 1). Azad *et al.*[33] indicated that there are two cubic polymorphs of $BaZr_{0.9}Y_{0.1}O_{3-\delta}$, with the α-form exhibiting a slightly lower unit cell and much lower protonic conductivity than the β-phase (Table 1). According to these authors, the difference in conductivity arises from a minor amount of Y occupying the A site in the β-polymorph, which reduces defect association and increases conductivity.

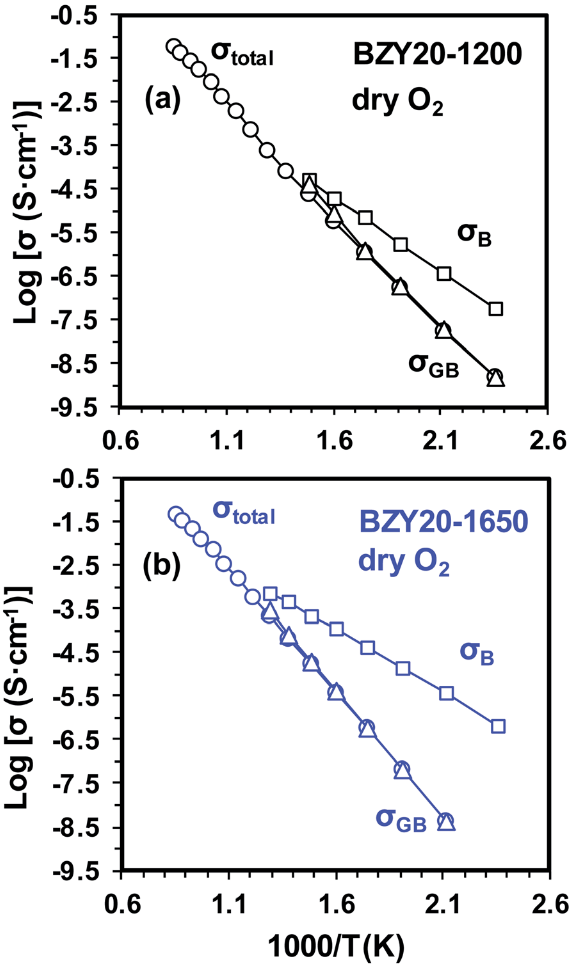

Fig. 7 Arrhenius representation of bulk (squares), total apparent grain boundary (triangles) and total conductivity (circles) in dry oxygen for (a) BZY20 sintered at 1200 °C (BZY20-1200) and (b) BZY20 sintered at 1650 °C (BZY20-1650).

It is well documented that the electrical conductivity of BZY-based phases in dry oxidising and moderately reducing atmospheres consists of contributions from oxygen vacancies and electron holes.[34] Whereas the oxygen-vacancy concentration in BZY20 is dominated by the extrinsic vacancies created by Y doping, the electron–hole concentration is highly affected by oxygen partial pressure, according to:

$$\frac{1}{2}O_2 + V_O^{\bullet\bullet} \leftrightarrow O_O^{\times} + 2h^{\bullet} \tag{6}$$

As a consequence, the contribution from electron holes to the total electrical transport is dependent on the oxidising character of the atmosphere, whereas the oxide-ionic contribution is practically independent of p_{O_2}. Fig. 8(a) and (b) show

Table 1 Total electrical conductivity at 600 °C of BZY20 samples prepared in the current work and $BaZrO_3$-based compositions previously reported in the literature

Composition	Sintering temperature (°C)	Conductivity ($S\ cm^{-1}$)	Atmosphere	Ref.
BZY20-1200	1200	1×10^{-3}	Wet N_2 ($p_{H_2O} \approx 0.022$ atm)	This work
BZY20-1650	1650	6.3×10^{-4}	Wet N_2 ($p_{H_2O} \approx 0.022$ atm)	This work
BZY20-1200	1200	1.5×10^{-3}	Wet O_2 ($p_{H_2O} \approx 0.022$ atm)	This work
BZY20-1650	1650	1.3×10^{-3}	Wet O_2 ($p_{H_2O} \approx 0.022$ atm)	This work
$BaZr_{0.8}Y_{0.8}O_{3-\delta}$	1675	4.2×10^{-3}	Wet 40%H_2 ($p_{H_2O} \approx 0.042$ atm)	34
$Ba_{0.97}Zr_{0.77}Y_{0.19}Zn_{0.04}O_{3-\delta}$	1325	1×10^{-3}	Wet 5%H_2/Ar ($p_{H_2O} \approx 0.03$ atm)	15
$BaZr_{0.85}Y_{0.15}O_{3-\delta}$	1800	$\approx 2 \times 10^{-4}$	Wet air ($p_{H_2O} \approx 0.03$ atm)	42
$BaZr_{0.9}Dy_{0.1}O_{3-\delta}$	1550	2×10^{-3} (bulk)	Wet Ar ($p_{H_2O} \approx 0.03$ atm)	43
$BaZr_{0.93}Y_{0.07}O_{3-\delta}$	1700	$\approx 5 \times 10^{-4}$	Wet air ($p_{H_2O} \approx 0.03$ atm)	44
$BaZr_{0.93}Y_{0.07}O_{3-\delta}$	1650	4×10^{-4}	Wet N_2 ($p_{H_2O} \approx 0.025$ atm)	45
$BaZr_{0.95}Y_{0.05}O_{3-\delta}$	1500–1650	1×10^{-3}	Dry H_2	46
$BaZr_{0.9}Y_{0.1}O_{3-\delta}$ ($Pm\bar{3}m$, 26% α + 74% β)	1500	$\approx 10^{-2}$	Wet 5%H_2/Ar ($p_{H_2O} \approx 0.03$ atm)	33
$BaZr_{0.9}Y_{0.1}O_{3-\delta}$ ($Pm\bar{3}m$, α)	1720	$\approx 10^{-3}$	Wet 5%H_2/Ar ($p_{H_2O} \approx 0.03$ atm)	33
$BaZr_{0.8}Y_{0.2}O_{3-\delta}$	1600	$\approx 7.9 \times 10^{-3}$	Wet N_2 ($p_{H_2O} \approx 0.031$ atm)	21
$BaZr_{0.85}Y_{0.15}O_{3-\delta}$	1350	$\approx 1 \times 10^{-3}$	Wet Ar ($p_{H_2O} \approx 0.03$ atm)	47
$BaZr_{0.9}Y_{0.1}O_{3-\delta}$ + Ni	1600	$\approx 1 \times 10^{-3}$	Wet 5%H_2/N_2 ($p_{H_2O} \approx 0.03$ atm)	48
$BaZr_{0.9}Y_{0.1}O_{3-\delta}$	1700	$\approx 2.3 \times 10^{-3}$	Wet 5%H_2/N_2 ($p_{H_2O} \approx 0.03$ atm)	48
$BaZr_{0.9}Y_{0.1}O_{3-\delta}$	2200	$\approx 3.4 \times 10^{-3}$	Wet 5%H_2/N_2 ($p_{H_2O} \approx 0.03$ atm)	48
$BaZr_{0.8}Y_{0.2}O_{3-\delta}$	1600	1.2×10^{-2}	Wet H_2 ($p_{H_2O} \approx 0.03$ atm)	49
$BaZr_{0.9}Y_{0.1}O_{3-\delta}$	1800	1.2×10^{-3}	Wet H_2 ($p_{H_2O} \approx 0.017$ atm)	50
$BaZr_{0.8}Y_{0.2}O_{3-\delta}$	1670	$\approx 3 \times 10^{-3}$	Wet H_2 ($p_{H_2O} \approx 0.03$ atm)	51
$BaZr_{0.9}Y_{0.1}O_{3-\delta}$	1800	9×10^{-3}	Wet air ($p_{H_2O} \approx 0.023$ atm)	52
$BaZr_{0.75}Sc_{0.25}O_{3-\delta}$	1250	$\approx 1.5 \times 10^{-3}$	Wet Ar ($p_{H_2O} \approx 0.025$ atm)	35
$BaZr_{0.8}Y_{0.2}O_{3-\delta}$	1250	$\approx 2 \times 10^{-3}$	Wet Ar ($p_{H_2O} \approx 0.025$ atm)	23

the temperature dependence of conductivity in dry N_2 and O_2 for BZY20-1200 and BZY20-1650, respectively. In the high-temperature range, the electrical conductivity is higher in O_2 for both samples, due to the greater concentration of electron holes (eqn (6)), which also has the effect of increasing the activation energy. However, at lower temperature, the equilibrium constant of the endothermic oxidation reaction (eqn (6)) decreases, and the electron–hole contribution to the electrical transport is lower. As a result, at low temperature, the electrical transport is principally ionic, and the conductivities in O_2 and N_2 converge.

Fig. 8(c) and (d) show the electrical conductivity in wet and dry nitrogen for BZY20-1200 and BZY20-1650. The higher conductivity in humid in comparison to dry conditions, observed in the low temperature range for both samples, is associated with the creation of proton transport carriers according to the exothermic hydration reaction:

$$H_2O + V_O^{\bullet\bullet} + O_O^{\times} \leftrightarrow 2OH_O^{\bullet} \tag{7}$$

With increasing temperature, both materials dehydrate and the protonic contribution in wet atmospheres decreases significantly.

It is notable that BZY20-1200 exhibits higher conductivity in wet N_2 in comparison to BZY20-1650, in the low-temperature range where protons dominate electrical transport, Fig. 9(a). This behaviour contrasts with the literature reports, in which samples with higher grain size present higher apparent grain-boundary conductivity and a concomitant higher total conductivity.[7] In the case of highly resistive $BaZrO_3$-based compositions, grain growth is usually promoted by thermal treatment to decrease the total contribution of grain boundaries to the electrical resistance.[7,23,35] Densification and grain growth was also achieved in BZY electrolyte by a co-sintering process over a $BaZr_{0.76}Ni_{0.04}Y_{0.2}O_{3-\delta}$ anode with an improved co-shrinkage procedure.[36] However, BZY20-1200 exhibits higher apparent grain-boundary conductivity in comparison to the analogue sintered at 1650 °C, in spite of the much lower grain size of the former, Fig. 9(b). This indicates that the low sintering temperature has a positive impact on the specific grain-boundary properties of the Zn-doped BZY20, as we discuss further below.

On the other hand, only minor differences in bulk conductivity between the samples were observed, with slightly higher values registered for BZY20-1650, Fig. 9(b). As mentioned earlier, the added Zn in the Ba-excess composition is expected to partly substitute on the B site, with Zn likely to be located in both grains and grain boundaries.[22] As the sintering temperature increases from 1200 to 1650 °C, it is probable that a greater concentration of Zn resides on the B position of the perovskite, acting as a dopant and increasing the oxygen-vacancy concentration. Although the location of more Zn on the B site in itself would independently be expected to lower the lattice parameter, as mentioned before, more Ba, from grain boundaries or undetected Ba-rich second phases, is expected to be incorporated on the A site at the higher sintering temperature of 1650 °C, with concomitant incorporation of more Y on the B position. Incorporation of both additional Zn and Y on the B site thus leads to a higher concentration of lower-valence cation and a greater oxygen-vacancy concentration in dry conditions.

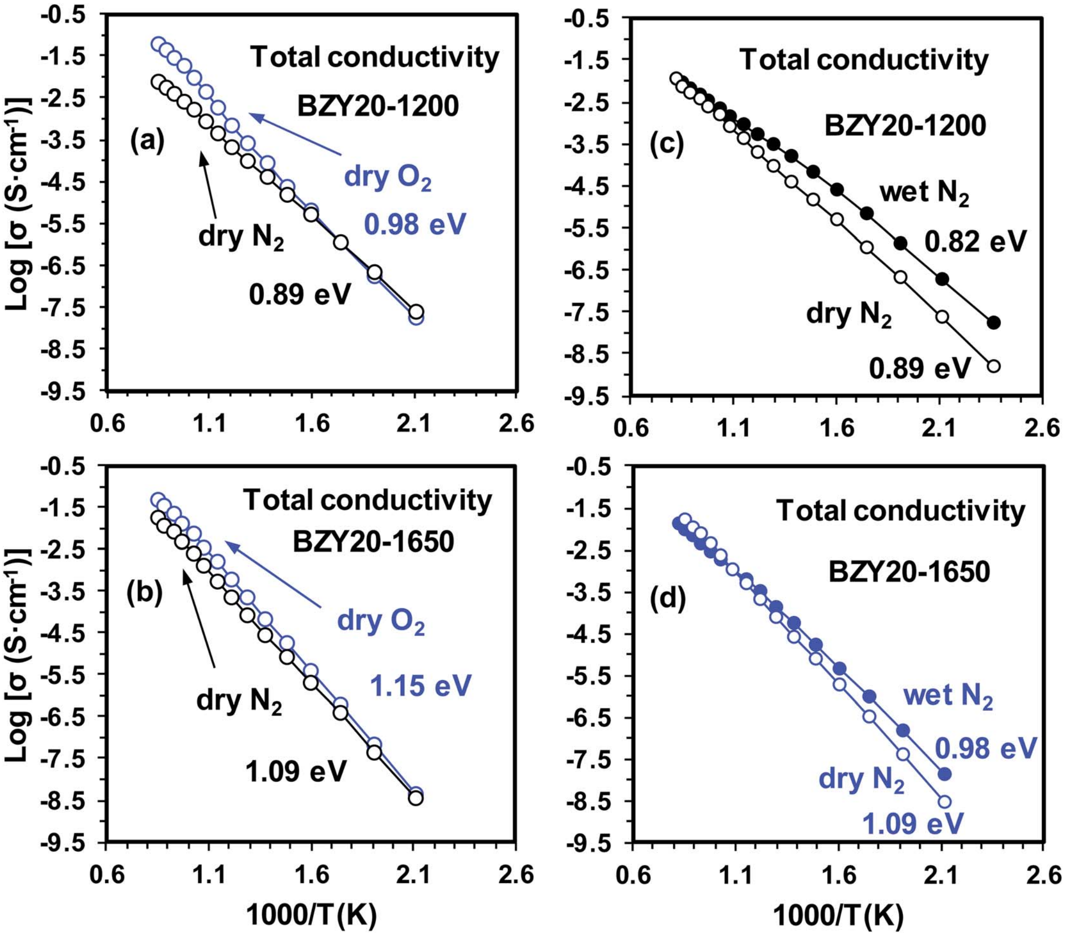

Fig. 8 Arrhenius dependence of total conductivity and associated activation energies at low temperature for (a and b) dry oxygen and dry nitrogen and (c and d) humidified nitrogen and dry nitrogen, for (a and c) BZY20 sintered at 1200 °C (BZY20-1200) and (b and d) BZY20 sintered at 1650 °C (BZY20-1650).

This, in turn, produces the slightly higher bulk conductivity observed for BZY20-1650 when oxygen vacancies are hydrated in wet N_2 (eqn (7)).

It was previously reported that a higher acceptor dopant content at the grain boundaries in BZY improves the grain-boundary conductivity[37,38] by lowering the space-charge potential.[39,40] It was later confirmed that the presence of ZnO at the

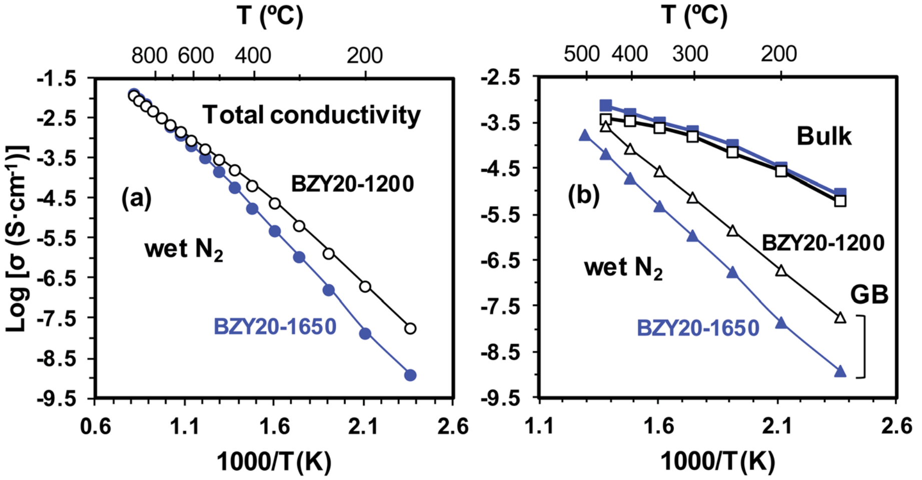

Fig. 9 Arrhenius representation of (a) total conductivity and (b) bulk (squares) and apparent grain-boundary conductivities (triangles) for BZY20-1200 (open symbols) and BZY20-1650 (closed symbols) in humidified nitrogen.

grain boundaries in BZY and $SrZr_{0.9}Y_{0.1}O_{3-\delta}$ also enhances the specific grain-boundary conductivity[22,41] as Zn segregation lowers the potential barrier height and brings about a higher concentration of positively charged species (protons and electron holes). Accordingly, in the present study, the greater degree of incorporation of Zn in the perovskite lattice on sintering at higher temperature (1650 °C) also modifies the grain-boundary properties. The lower concentration of Zn in the grain boundary region for BZY20-1650 is expected to increase the space-charge potential and, as a consequence, the specific grain-boundary resistance increases.

It is notable that, although apparent differences in total conductivity were obtained at low temperature for BZY20-1200 and BZY20-1650, similar values were obtained in the high-temperature range, regardless of the sintering temperature, due to the expected dominance of the bulk component with increasing temperature.

4. Conclusions

Lowering the sintering temperature of barium zirconate-based proton conductors is essential for their widespread incorporation in electrochemical devices. It is demonstrated that a combination of sinter-reactive nanopowder, Ba excess and ZnO sintering aid can effectively lower the sintering temperature of $BaZr_{0.8}Y_{0.2}O_{3-\delta}$ to 1200 °C, achieving a relative density of 98% with a soak time of 4 hours. This lower sintering temperature avoids problems of BaO loss which occur above 1250 °C and facilitates co-sintering with other cell components, in addition to deriving cost and energy-saving benefits.

The sinter-reactive powders were prepared as BZY perovskite with Ba excess at 750 °C and can be adapted to thin-film deposition with still lower processing temperatures. In bulk ceramic form, the sintering temperature of 1200 °C provided a grain size of ~200 nm, which is shown to be sufficiently large to provide a comparable electrical performance to micrograined material sintered at 1650 °C. Although the bulk conductivity of the micrograined sample is slightly higher above 500 °C, the specific grain-boundary conductivity for BZY20 densified at low temperature is much higher than that of the micrograined analogue, leading to higher total conductivities below ~500 °C for the material processed at 1200 °C.

Conflicts of interest

There are no conflicts to declare.

Acknowledgements

We thank MICINN in Spain for financial support through projects RTI2018-095088-B-I00, RTI2018-095373-J-100 and predoctoral grant BES-2016-077023. DPF also thanks the FCT (Fundação para a Ciência e a Tecnologia, grants numbers PTDC/QUI-ELT/3681/2020, POCI-01-0145-FEDER-032241, UIDB/00481/2020 and UIDP/00481/2020) and the Centro Portugal Regional Operational Programme (Centro2020), under the PORTUGAL 2020 Partnership Agreement, through the European Regional Development Fund (ERDF), grant number CENTRO-01-0145-FEDER-022083. We acknowledge support of the publication fee by the CSIC (Spain) Open Access Publication Support Initiative through its Unit of Information Resources for Research (URICI).

References

1 H. G. Bohn and T. Schober, *J. Am. Ceram. Soc.*, 2000, **72**, 768–772.
2 K. D. Kreuer, *Annu. Rev. Mater. Res.*, 2003, **33**, 333–359.
3 C. Duan, R. J. Kee, H. Zhu, C. Karakaya, Y. Chen, S. Ricote, A. Jarry, E. J. Crumlin, D. Hook, R. Braun, N. P. Sullivan and R. O'Hayre, *Nature*, 2018, **557**, 217–222.
4 Y. Yamazaki, R. Hernandez-Sanchez and S. M. Haile, *J. Mater. Chem.*, 2010, **20**, 8158–8166.
5 A. Magrez and T. Schober, *Solid State Ionics*, 2004, **175**, 585–588.
6 P. Babilo, T. Uda and S. M. Haile, *J. Mater. Res.*, 2011, **22**, 1322–1330.
7 Y. Yamazaki, R. Hernandez-Sanchez and S. M. Haile, *Chem. Mater.*, 2009, **21**, 2755–2762.
8 J. Tong, D. Clark, L. Bernau, M. Sanders and R. O'Hayre, *J. Mater. Chem.*, 2010, **20**, 6333–6341.
9 N. Ito, H. Matsumoto, Y. Kawasaki, S. Okada and T. Ishihara, *Solid State Ionics*, 2008, **179**, 324–329.
10 P. Babilo and S. M. Haile, *J. Am. Ceram. Soc.*, 2005, **2368**, 2362–2368.
11 S. Tao and J. T. S. Irvine, *Adv. Mater.*, 2006, **18**, 1581–1584.
12 S. Ricote and N. Bonanos, *Solid State Ionics*, 2010, **181**, 694–700.
13 J.-S. Park, J.-H. Lee, H.-W. Lee and B.-K. Kim, *Solid State Ionics*, 2010, **181**, 163–167.
14 Z. Zhao, J. Gao, Y. Meng, K. S. Brinkman and J. Tong, *Ceram. Int.*, 2021, **47**, 11313–11319.
15 S. Tao and J. T. S. Irvine, *J. Solid State Chem.*, 2007, **180**, 3493–3503.
16 Á. Triviño-Peláez, G. C. Mather, D. Pérez-Coll, M. Aparicio and J. Mosa, *J. Sol-Gel Sci. Technol.*, 2020, **95**, 661–669.
17 G. Gorni, M. J. Pascual, A. Caballero, J. J. Velázquez, J. Mosa, Y. Castro and A. Durán, *J. Non-Cryst. Solids*, 2018, **501**, 145–152.
18 J. Rodriguez-Carvajal, *Phys. B*, 1993, **192**, 55–69.
19 B. J. T. S. Irvine, D. C. Sinclair and A. R. West, *Adv. Mater.*, 1990, 132–138.
20 V. G. Kessler, *Handbook of Sol-Gel Science and Technology*, 2017.
21 P. Babilo, T. Uda and S. M. Haile, *J. Mater. Res.*, 2007, **22**, 1322–1330.
22 H. S. Soares, I. Antunes, F. J. A. Loureiro, D. Pérez-Coll, M. G. Willinger, A. D. Brandão, G. C. Mather and D. P. Fagg, *Int. J. Hydrogen Energy*, 2021, **46**, 26466–26477.
23 R. B. Cervera, Y. Oyama, S. Miyoshi, K. Kobayashi, T. Yagi and S. Yamaguchi, *Solid State Ionics*, 2008, **179**, 236–242.
24 D. Han, Y. Nose, K. Shinoda and T. Uda, *Solid State Ionics*, 2012, **213**, 2–7.

25 G. C. Mather, S. García-Martín, D. Benne, C. Ritter and U. Amador, *J. Mater. Chem.*, 2011, **21**, 5764–5773.

26 J. M. Polfus, M. L. Fontaine, A. Thøgersen, M. Riktor, T. Norby and R. Bredesen, *J. Mater. Chem. A*, 2016, **4**, 8105–8112.

27 Á. Triviño-Peláez, D. Pérez-Coll, J. Mosa, C. Ritter, U. Amador and G. C. Mather, *J. Power Sources*, 2021, **493**, 3229691.

28 J. M. Polfus, B. Yildiz, H. L. Tuller and R. Bredesen, *J. Phys. Chem. C*, 2018, **122**, 307–314.

29 C. Kjølseth, H. Fjeld, Ø. Prytz, P. I. Dahl, C. Estournès, R. Haugsrud and T. Norby, *Solid State Ionics*, 2010, **181**, 268–275.

30 A. Magrasó, C. Kjølseth, R. Haugsrud and T. Norby, *Int. J. Hydrogen Energy*, 2012, **37**, 7962–7969.

31 J. T. S. Irvine, D. C. Sinclair and A. R. West, *Adv. Mater.*, 1990, **2**, 132–138.

32 J. Fleig, *Solid State Ionics*, 2000, **131**, 117–127.

33 A. K. Azad, C. Savaniu, S. Tao, S. Duval, P. Holtappels, R. M. Ibberson and J. T. S. Irvine, *J. Mater. Chem.*, 2008, **18**, 3414–3418.

34 K. Nomura and H. Kageyama, *Solid State Ionics*, 2007, **178**, 661–665.

35 R. B. Cervera, Y. Oyama, S. Miyoshi, I. Oikawa, H. Takamura and S. Yamaguchi, *Solid State Ionics*, 2014, **264**, 1–6.

36 L. Bi, E. H. Da'as and S. P. Shafi, *Electrochem. Commun.*, 2017, **80**, 20–23.

37 M. Shirpour, R. Merkle and J. Maier, *Solid State Ionics*, 2012, **225**, 304–307.

38 M. Shirpour, B. Rahmati, W. Sigle, P. A. Van Aken, R. Merkle and J. Maier, *J. Phys. Chem. C*, 2012, **116**, 2453–2461.

39 C.-T. Chen, C. E. Danel and S. Kim, *J. Mater. Chem.*, 2011, **21**, 5435.

40 F. Iguchi, N. Sata and H. Yugami, *J. Mater. Chem.*, 2010, **20**, 6265.

41 G. Heras-juaristi, D. Pérez-Coll and G. C. Mather, *J. Power Sources*, 2016, **331**, 435–444.

42 V. P. Gorelov, V. B. Balakireva and A. V. Kuz'Min, *Russ. J. Electrochem.*, 2010, **46**, 890–895.

43 S. Ricote, L. Krishna, W. G. Coors and J. R. O'Brien, *Solid State Ionics*, 2018, **314**, 25–29.

44 V. P. Gorelov, V. B. Balakireva, Y. N. Kleshchev and V. P. Brusentsov, *Inorg. Mater.*, 2001, **37**, 535–538.

45 W. Wang and A. V. Virkar, *J. Power Sources*, 2005, **142**, 1–9.

46 H. Iwahara, T. Yajima, T. Hibino, K. Ozaki and H. Suzuki, *Solid State Ionics*, 1993, **61**, 65–69.

47 H. W. Kim, J. Seo, J. H. Yu, K. S. Yun, J. H. Joo, J. Moon and H. J. Park, *Ceram. Int.*, 2021, **47**(23), 32720–32726.

48 S. Ricote, N. Bonanos, A. Manerbino, N. P. Sullivan and W. G. Coors, *J. Mater. Chem. A*, 2014, **2**, 16107–16115.

49 D. Han, K. Toyoura and T. Uda, *ACS Appl. Energy Mater.*, 2021, **4**, 1666–1676.

50 K. Katahira, Y. Kohchi, T. Shimura and H. Iwahara, *Solid State Ionics*, 2000, **138**, 91–98.

51 S. S. Baek, K. Y. Park, T. H. Lee, N. Lee, Y. Seo, S. J. Song and J. Y. Park, *Acta Mater.*, 2014, **66**, 273–283.

52 F. Iguchi, N. Sata, T. Tsurui and H. Yugami, *Solid State Ionics*, 2007, **178**, 691–695.